



# Manufacturing and evaluation of a multi-purpose Iranian head and neck anthropomorphic phantom called MIHAN

Mohammad Ahmadi<sup>1</sup> · Meysam Ramezani Anarestani<sup>2</sup> · Sanaz Hariri Tabrizi<sup>1</sup> · Zohreh Azma<sup>1</sup>

Received: 28 October 2020 / Accepted: 13 June 2021 / Published online: 16 July 2021  
© International Federation for Medical and Biological Engineering 2021

## Abstract

A new multi-purpose Iranian head and neck (MIHAN) anthropomorphic phantom was designed and manufactured to be used in diagnostic and therapeutic applications. Geometry of MIHAN phantom was determined based on the average dimensions acquired by CT scans of twenty patients without any medical problems in their head and neck site. Because the phantom was expected to be used with different modalities with a wide range of photon energies, attenuation coefficients of some selected materials were determined using Monte Carlo simulation. Based on analytical and simulation results, acrylonitrile butadiene styrene (ABS) and polylactic acid (PLA) were found suitable choices for soft and bony tissues, respectively. They were used in the 3D printer to build the phantom. The suitability of the materials was checked by CT number value comparison between the organs included in the phantom and the corresponding body tissues and also film dosimetry of a typical intensity-modulated radiation therapy (IMRT) plan. Hounsfield Unit agreement and  $95\% \pm 2\%$  pass rate for the IMRT plan verification proved the suitability of material selection. Also, the film dosimetry showed feasibility of using MIHAN in radiotherapy plan verification workflow. In addition, PLA was introduced as a spongy bone tissue substitute for the first time.

**Keywords** Anthropomorphic phantom · Dosimetry · Radiation therapy · Nuclear medicine · Tissue-equivalent

## Glossary

Symbol	Name	Definition	Unit
$\mu$	Attenuation coefficient	Total linear attenuation coefficient	$\text{cm}^{-1}$
$E_{\text{eff}}$	Effective energy	Effective energy of the irradiated photon	keV

## 1 Introduction

Tissue-equivalent anatomical phantoms play an essential role in radiation protection, radiobiology, calibration of radiation devices, dose distribution verification in radiation therapy, and to develop and test new imaging modalities.

The composition of a tissue substitute chosen for a phantom is selected based on the composition of the body tissue and characteristics of the radiation field [1]. Dosimetry of the heterogeneous body organs is more difficult than the homogenous ones. Head and neck (H&N) region with the skull, vertebra and face bones, and several air cavities, is one of these challenging body sites. Several commercial and non-commercial H&N phantoms with simple cylindrical to complicated geometries have been introduced and used in the clinical settings [2–14]. While the phantoms with simple cylindrical geometry permit them to be used for a range of clinical body sites, they are not an ideal analogy for the H&N site. Because water is still a standard substance of choice for radiology and radiotherapy dosimetry, some of the developed phantoms have been designed as a hollow shell that can be filled with water or other materials [3, 7]; or in the form of solid water-equivalent slabs [5, 6, 8]; or hollow cylindrical phantoms [2, 4, 9, 10]. Most of them have been developed for one or a defined number of purposes or they provide no or limited available sites to insert desirable organs or include a few number of heterogeneous organs. These limitations restrict their use in different clinical scenarios and increase the clinical costs. Providing

✉ Sanaz Hariri Tabrizi  
S\_HaririTabrizi@sbu.ac.ir

<sup>1</sup> Department of Medical Radiation Engineering, Shahid Beheshti University, Tehran, Iran

<sup>2</sup> Department of Radiation Application, Shahid Beheshti University, Tehran, Iran

a multi-purpose phantom will speed up the dosimetry procedures and give the flexibility in dosimeter selection based on the desired removable 3D-printed detector holders and required resolution and accuracy. The mass or linear attenuation coefficients ( $\mu$ ) of each organ in the phantom should approximate the real one [1]. There are several methods for the selection of the most suitable materials for manufacturing a tissue-equivalent phantom via  $\mu$  matching. They include Monte Carlo simulation [15], CT number (Hounsfield unit — HU) matching [16], or dosimetry of a pre-determined treatment plan [7, 8].

Herein, a hollow multi-purpose Iranian head and neck (MIHAN) anthropomorphic phantom that can be filled with water and also have the possibility of inserting different H&N organs is introduced. It can be used for radiotherapy quality assurance (QA) purposes, radioiodine dosimetry [17], nuclear accident assessments, calibration/validation of different molecular imaging modalities, testing reconstruction or artifact reduction algorithms, and image distortion evaluations. The phantom incorporates optional 3D-printed heterogeneities, and it includes holders for the insertion of radiochromic films and thermoluminescent detectors (TLDs) for dosimetry purposes. To the best of author's knowledge, correspondence between the printer materials and soft and bony tissues is evaluated in this study for the first time. It provides flexibility to insert new heterogeneities and dosimeters in the phantom. Because the organ sizes differ among different nations [18], a national hollow H&N phantom based on healthy Iranian people was developed. Herein, the phantom preparation, design, construction, and evaluation steps were presented, and attenuation characteristics of the MIHAN phantom for a wide range of photon energies were investigated. Then suitability of the constructed phantom for quality assurance purposes in intensity-modulated radiotherapy (IMRT) was evaluated by using radiochromic film.

## 2 Materials and methods

### 2.1 Determination of phantom geometry

The geometry of MIHAN anthropomorphic phantom was determined based on segmentation of important organs on the CT scan images of 20 patients referred for medical assessment at Shohada Tajrish Hospital (10 males and 10 females with an age range of  $48 \pm 14$  years and head diameter of  $167 \pm 13$  mm) who did not have any problem in their H&N region. Size and position of the internal body structures, including the thyroid gland, spinal canal, cervical vertebra, nasal cavity, mandible, glottic larynx, and trachea, was determined by averaging data obtained from segmenting the desired organs at ISOgray TPS® (DOSIsoft, France). Figure 1 shows a typical three-dimensional (3D) reconstruction



**Fig. 1** 3D representation of segmented organs in ISOgray treatment planning system including the thyroid gland (yellow), mandible (purple), and nasal cavity, paranasal and ethmoid sinus (green)

of the thyroid gland, mandible, and nasal cavity contours in a patient.

### 2.2 Selection of phantom material

In order to mimic the radiation attenuation properties of human tissue, materials of the phantom must be chosen in a way that has as close electron density and effective atomic number as possible to body tissues. The materials presented in Table 1 include some of the common materials to substitute soft tissue and bone. The presented values were calculated based on the data provided by Nguyen et al. and Wagner [19, 20] and equations presented in [21].

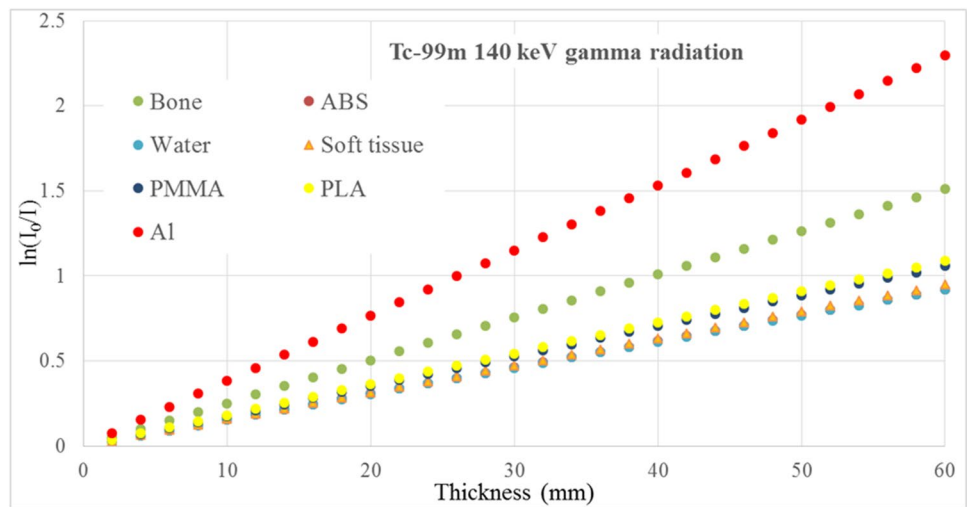
Polymethyl methacrylate (PMMA) is a common material of choice as equivalent to soft tissue [1, 3–6] and aluminum as equivalent to bone [1–4]. There are different methods for

**Table 1** Mass and electron density and effective atomic number of some common materials for phantom design\* [21]

Material	Electron density $\times 10^{23}$ (e/g)	Effective atomic number	Mass density (g/cm <sup>3</sup> )
Bone	3.19	12.31	1.65
Al	2.90	13.00	2.70
PLA	3.18	6.82	1.25
Soft tissue	3.31	7.64	1.04
Water	3.34	7.51	1.00
PMMA	3.25	6.47	1.19
ABS	3.27	5.76	1.03–1.38

\* Al aluminum, PLA polylactic acid, PMMA polymethyl methacrylate (Plexiglas), ABS acrylonitrile butadiene styrene.

**Fig. 2** Logarithm of blank to detected current through different materials for Tc-99 m gamma rays



phantom manufacturing such as molding [7], use of water equivalent slabs [5, 6, 9], and 3D printing [3, 8, 10]. Due to flexibility provided by 3D printing method, the two common filament materials, namely acrylonitrile butadiene styrene (ABS) and polylactic acid (PLA), are presented in Table 1. SolidWorks (Dassault Systèmes Co.) software was used for the phantom design, and 3D printing was done using a fused deposition modeling (FDM) printer. ABS has been used as a surrogate for the soft tissue [3, 8, 22], whereas PLA has been considered as the brain tissue [23], lung, fat, and muscle by adjusting its infill densities [14] or the thyroid [15]. Based on the fact that MIHAN phantom was intended to be used in radiotherapy and nuclear medicine applications with a predominant photon energy range of more than 100 keV, especially a few MeV, Compton scattering and therefore the electron density were the main factors to be taken into account [1]. Agreement between electron density of ABS to soft tissue (1.2%) and PLA to bone tissue (0.3%) encouraged us to manufacture the phantom by 3D printing method. Afterwards, a thorough investigation of  $\mu$  matching of the materials mentioned above was done by the Monte Carlo (MC) code MCNPX 2.6.0.

**2.3 MC-based confirmation of material selection**

MC simulation was used to obtain the linear attenuation coefficient of the materials presented in Table 1 for different photon energy spectra expected to be used in MIHAN phantom manufacturing. The bone and soft tissue compositions and densities were simulated based on the ICRP phantom. Five photon energy spectra were considered including Tc-99 m (140 keV), F-18 (511 keV) radionuclides utilized in nuclear medicine, I-131 spectra [24] for radioiodine therapy, 6 MV X-ray photons to simulate VARIAN radiotherapy linear accelerator (Linac) energy spectrum [25], and 120 kVp X-ray photons used in CT scan [26]. Their effective energy

was calculated based on Eq. 1 to find the trend of  $\mu$  versus effective energy.

$$E_{\text{eff}} = \frac{\sum \varphi_i E_i}{\sum \varphi_i} \tag{1}$$

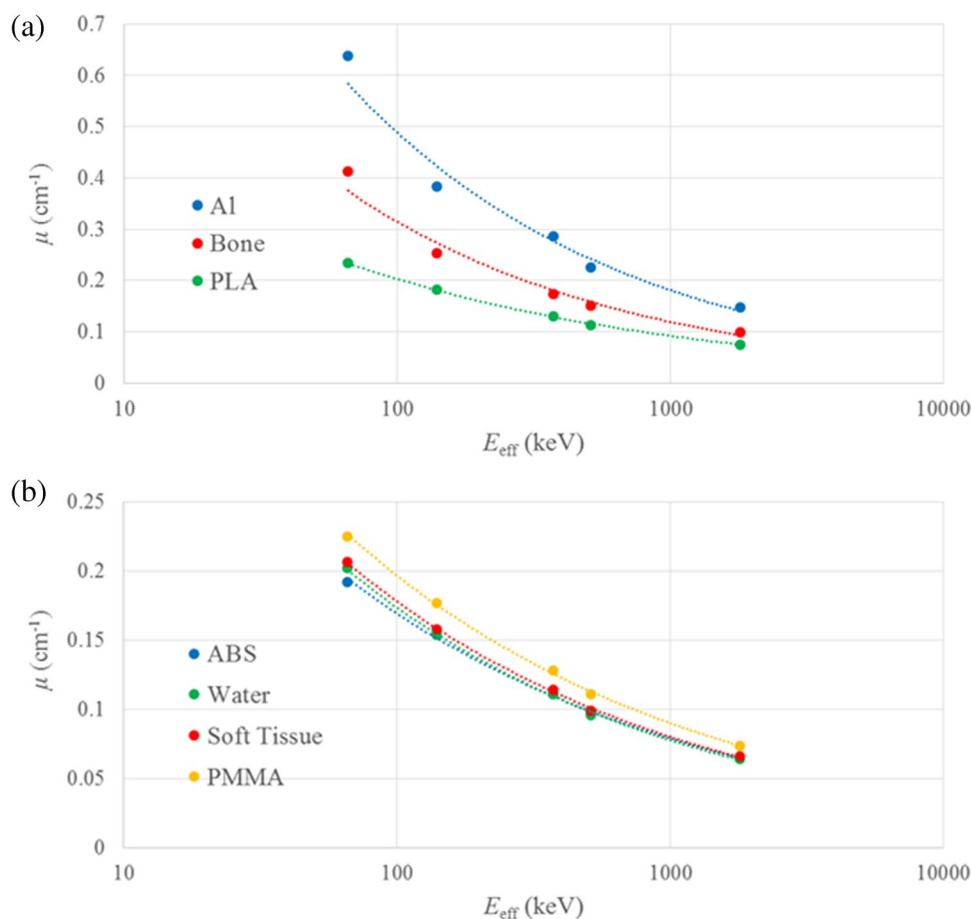
where  $\varphi_i$  is the fluence rate in  $i$ th energy bin of  $E_i$ . Therefore, the obtained effective photon energies were calculated as 66, 140, 373, 511, and 1798 keV for CT, Tc-99 m, I-131, F-18, and Linac, respectively.

Sixty  $10 \times 10 \text{ cm}^2$  slabs with 1-mm thickness from each material was simulated in a good geometry irradiation configuration. The slabs were positioned in vacuum between a point mono-directional photon source and a semi-point ( $8 \times 10^{-12} \text{ mm}^3$ ) detector with a 20 cm source to detector distance. The slabs were positioned in the radiation field one by one. Therefore, for each material and photon energy spectrum, 60 MC simulations were run, and the photon current on the front surface of the detector was recorded. For each thickness, 200,000 histories were transported to achieve an error of less than 1% within a few minutes. Using the Beer-Lambert law, the  $\mu$  values were found by fitting the data points for each material and source effective energy. Figure 2

**Table 2** Comparison of the attenuation coefficients of water and aluminum obtained from the simulation and the NIST data [27, 28] for the 140 and 511 keV photon energies

E(keV)	NIST $\mu(\text{cm}^{-1})$	Simulation $\mu(\text{cm}^{-1})$	Difference (%)
<b>Aluminum</b>			
140	0.384	0.383	- 0.2
511	0.225	0.226	0.4
<b>Water</b>			
140	0.151	0.154	2.0
511	0.095	0.096	1.0

**Fig. 3** Comparison of the attenuation coefficients for **a** aluminum (Al), bone, and PLA and **b** ABS, water, soft tissue, and PMMA for different energies



shows the logarithm of primary current to the detected one versus attenuator thickness for 140 keV gamma radiation emitted by Tc-99 m. Fitting a linear equation to the data points resulted in the slope of the lines from which the  $\mu$  values were deduced. In order to validate the simulation, calculated attenuation coefficients for water and aluminum were compared to their counterparts available at the NIST website [27, 28] for 140 and 511 keV monoenergetic photons.

### 2.4 Film dosimetry

Gafchromic EBT2 film dosimeter was used to evaluate the applicability and suitability of the manufactured phantom in dosimetry applications. Nineteen  $1.5 \times 1.5 \text{ cm}^2$  pieces of film were exposed using 6 MV X-ray emerged from Unique Varian Linac (Varian medical systems, Palo Alto, CA, USA) for a dose range of 0.5 to 9.5 Gy in 0.5 Gy steps. The dose ( $D$ ) calibration curve was calculated from the obtained net optical density (NOD) based on the Devic protocol [29] according to the following equation with 1.2% uncertainty (Eq. 2).

$$D(\text{Gy}) = 518.2\text{NOD}^{3.5} + 16.69\text{NOD} \tag{2}$$

Afterwards, CT images were taken by Ingenuity Core CT scanner (Koninklijke Philips co.) from the phantom using the system settings of 120 kVp and 500 mA and slice thickness of 3 mm. Delineation of a hypothetical planning target volume (PTV) was performed as a cylinder with a radius of 2.5 cm and parotid gland as a healthy tissue close to the PTV. An intensity-modulated radiation therapy (IMRT) plan was prepared using five equidistance 6 MV radiation fields with the prescription dose value of 2 Gy per fraction by Eclipse treatment planning

**Table 3** Fitting parameters of Eq. 3 for different materials as well as their 95% CI. The goodness of fit is indicated as  $R^2$  value.\*

Material	$a$	95% CI for $a$	$b$	95% CI for $b$	$R^2$
Bone	2.98	2.06	-0.48	0.14	0.9805
Al	4.59	3.55	-0.48	0.16	0.9759
PLA	0.98	0.08	-0.34	0.02	0.9994
Soft tissue	0.90	0.08	-0.35	0.02	0.9994
Water	0.88	0.08	-0.35	0.02	0.9993
PMMA	0.93	0.10	-0.34	0.02	0.9991
ABS	0.76	0.10	-0.33	0.03	0.9984

\* Al aluminum, PLA polylactic acid, PMMA polymethyl methacrylate (Plexiglas), ABS acrylonitrile butadiene styrene.

**Table 4** Average  $\pm$  standard deviation of dimensions of delineated organs on CT images of 20 healthy individuals

Organ	Diameters (mm)			Heights (mm)		Thickness (mm)	Volume (cm <sup>3</sup> )	
	Neck	Trachea	Spinal canal	Left thyroid	Right thyroid	Thoracic vertebra	Thyroid gland	Mandible
Dimensions	127 $\pm$ 1	15 $\pm$ 2	10 $\pm$ 1	32 $\pm$ 7	34 $\pm$ 8	43 $\pm$ 7	15 $\pm$ 4	61 $\pm$ 1

system (TPS) (Varian medical systems, Palo Alto, CA, USA) [30]. Configuration of the fields was in such a way that the rays passed through the bone and air inhomogeneities in their paths. The phantom was irradiated while six 5.7  $\times$  5.7 cm<sup>2</sup> film pieces were positioned inside the film holder of the phantom. The comparison of the TPS calculated total dose with the measured dose derived from the film pieces was done using the gamma index method [31]. The acceptance criteria were a dose-difference criterion of 3% and distance-to-agreement (DTA) criterion of 3 mm. The ratio of the number of pixels with the gamma index equal to or less than one to the total number of embraced pixels within a 50% isodose curve was determined.

### 3 Results and discussion

#### 3.1 Phantom material

Fitting linear equations to curves presented in Fig. 2 and finding their slope resulted in the linear attenuation coefficients of different materials for different energy spectra presented in Sect. 2.3. All the obtained fitting R-squared values were more than 0.9980. Table 2 shows the results of validating the

obtained values compared to the NIST database for the two monochromatic photon emitters in aluminum and water. The difference between the calculated and the NIST attenuation coefficients was not greater than 2% which confirmed the validity of the simulation.

Illustration of the  $\mu$  values versus the effective energies implied a power-law equation fitting to the data points as indicated in Eq. (3).

$$\mu = aE_{\text{eff}}^b \tag{3}$$

in which  $\mu$  is the total linear attenuation coefficient in cm<sup>-1</sup>,  $E_{\text{eff}}$  is the effective energy of the irradiated photon in keV and  $a$  and  $b$  are the fitting parameters. Figure 3 shows the  $\mu$  values versus effective energy for bone, aluminum, PLA, soft tissue, water, PMMA, and ABS and their fits. It can be seen that PLA can surrogate the bone tissue better than aluminum for the energy range from 66 keV effective energy of CT scanner to about 1.8 MeV effective energy of radiotherapy X-ray photons. The largest difference between bone and aluminum was about 2.6 times the difference between PLA and bone for I-131 energy spectra. It can be seen that the discrepancy is more pronounced for lower energies which limit the use of bone surrogates. It is due to the

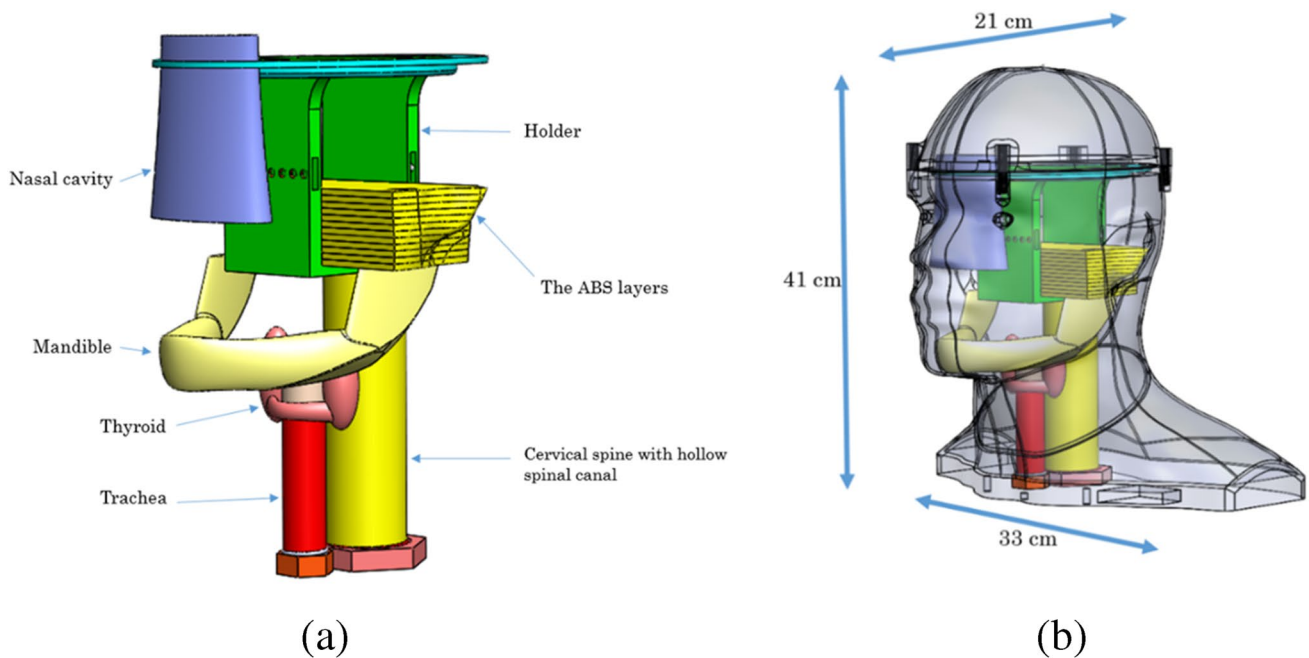
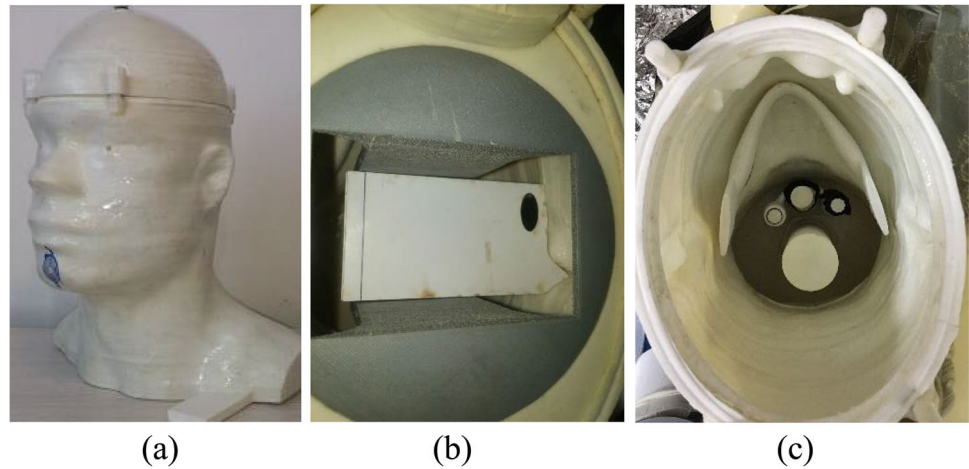


**Fig. 4** **a** Internal parts of the MIHAN phantom, **b** the whole phantom including the outer shell and dimensions



**Fig. 5** **a** A photo from the MIHAN phantom with a marker on the chin for CT scanning. Internal view of the phantom (b) with and (c) without the film holder. **b** Trail of the mandible can be seen as a black PLA ellipse and the right curvature is for conforming the ear and recording the parotid dose. **c** Cervical spine, trachea, thyroid lobes, and mandible can be seen inside the phantom



fact that photoelectric interaction which depends strongly on the atomic number is dominant in lower energies, and based on Table 1, this difference is about 45% between bone and PLA. However, increase of the energy results in Compton scattering interaction dominance which depends on the electron density with a difference of less than 1% for bone and PLA.

On the other hand, while water shows the most similar behavior to the soft tissue, ABS is a better representative of the soft tissue than the ubiquitous PMMA material. Based on Table 1, larger difference is between the effective atomic number of soft tissue and other materials than the electron density. Similar to bone, increase of the effective energy decreases the difference between the soft tissue and other materials. The largest difference between ABS and soft tissue was about 7%, while the smallest difference between PMMA and soft tissue was about 9%. Therefore, manufacturing the phantom using the 3D printer using ABS and PLA filaments in place of soft tissue and bone was confirmed.

Table 3 shows the calculated fitting parameters to Eq. 3 and their 95% confidence interval (CI) as well as their coefficients of determination ( $R^2$ ). Because of the large energy

range used in this study (more than two orders of magnitude), it is expected that the fitting parameters can be used for the extrapolated energies, too. Because PLA can act as the spongy bone (discussed in Sect. 3.3), its fitting parameters are not so different from the soft tissue and its substitutes. However, the PLA curve is located above the PMMA.

The MIHAN phantom was constructed to be used in transmission and emission tomography and even magnetic resonance imaging (MRI) image analyses. It is due to the fact that the attenuation coefficients of the phantom materials agree with human tissue for a wide range of energy spectrum and it does not include any ferromagnetic material.

### 3.2 Phantom geometry

Table 4 presents the mean and standard deviation of the dimensions and volumes obtained from segmentation of organs of interest in 20 healthy individuals.

The phantom was manufactured as a hollow ABS shell with a thickness of 2 mm to fill in with water and desired dosimeters and internal body organs. The internal organs and external shell of the phantom were manufactured based on the mean

**Fig. 6** Comparison of a CT slice of the MIHAN phantom (a) to a typical slice of the neck region of a patient (b). Three ROIs in the thyroid, cervical spine bone, and soft tissue are indicated to calculate the statistical measures of the HUs and the corresponding areas

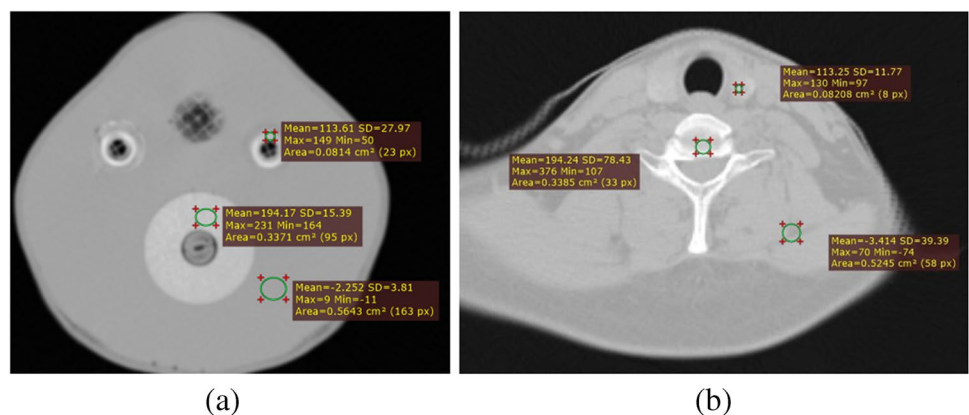


**Table 5** Comparison of the CT numbers obtained from the MIHAN phantom and corresponding values in a patient shown in Fig. 6. The mean ± standard deviation of the HUs and ROI areas are presented

MIHAN phantom			Patient		
ROI	HU	Area (cm <sup>2</sup> )	ROI	HU	Area (cm <sup>2</sup> )
PLA	194 ± 15	0.34	Bone	194 ± 78	0.34
Water	-2 ± 4	0.56	Soft tissue	-3 ± 39	0.52
ABS	114 ± 28	0.08	Thyroid	113 ± 12	0.08

values presented in Table 4. The internal organs were manufactured from ABS as a substitute for the soft tissue and PLA for the bony structures. The trachea was made of ABS, and it was hollow. Two hollow ABS thyroid lobes and an isthmus in between were manufactured in order to inject radioiodine for dosimetry purposes and monitoring [17]. The nasal cavity and mandible were manufactured from PLA, while the former was hollow and the latter one was filled. All the hollow internal organs have a thickness of 2 mm. The cervical spine and trachea were screwed to the bottom surface of the phantom, and the thyroid was fastened to the trachea. The size of the phantom along coronal, sagittal, and transverse planes were 21 × 33 × 41 cm<sup>3</sup> whose mass after filling with water was 6.5 kg. Figure 4 shows a schematic diagram of the internal parts of the phantom and their position in situ.

Four screws in the skull enclosed the reservoir, while a hole on top of the head lets the user to fill it with water. The phantom was designed in such a way to allow the user to measure the dose distribution using radiochromic films and TLDs. The film holder comprised eleven ABS slabs with 3-mm thickness. For the slabs intersecting the mandible, PLA inserts were positioned following the mandible curvature (Fig. 5b). Film holders can rotate in 360 degrees and can be aligned with any Cartesian axes to record the 2D dose distribution in any plane and reconstruct the 3D dose distribution. TLDs can be used for measuring absorbed dose in eye globs, pharynx, clavicle, and cervical spinal cord by two types of TLD (TLD-100 and GR-200). The TLD holder in the spinal canal was manufactured from ABS with TLD position center to center distance of 5 mm. In order to record the absorbed dose in the pharynx, a TLD position was situated on top of the trachea. Herein, the film dosimetry of the phantom has been reported and no TLD measurement was performed. Figure 5 shows three photos of the MIHAN phantom.

### 3.3 Phantom evaluation

In order to double check the validity of material selection after printing, the CT number values of the manufactured phantom were compared to a patient. Figure 6 shows a slice of the phantom as well as the head region of a patient side by side. Three regions of interest (ROI) in the bone and soft tissue parts are shown on the phantom and the human CT images. The corresponding mean and standard deviation of the obtained HUs and corresponding areas are indicated in Table 5. The PLA material which was used for the first time to simulate the human bone showed nearer HU value to real spongy bone compared to a similar study [16].

Applicability of the MIHAN phantom was tested through its application in a radiotherapy verification setting. Implementing a typical H&N IMRT plan and comparing the film measurements to the calculated treatment plans resulted in the gamma pass rates presented in Table 6. The region enclosed by the calculated 50% isodose line was used to report the pass rates.

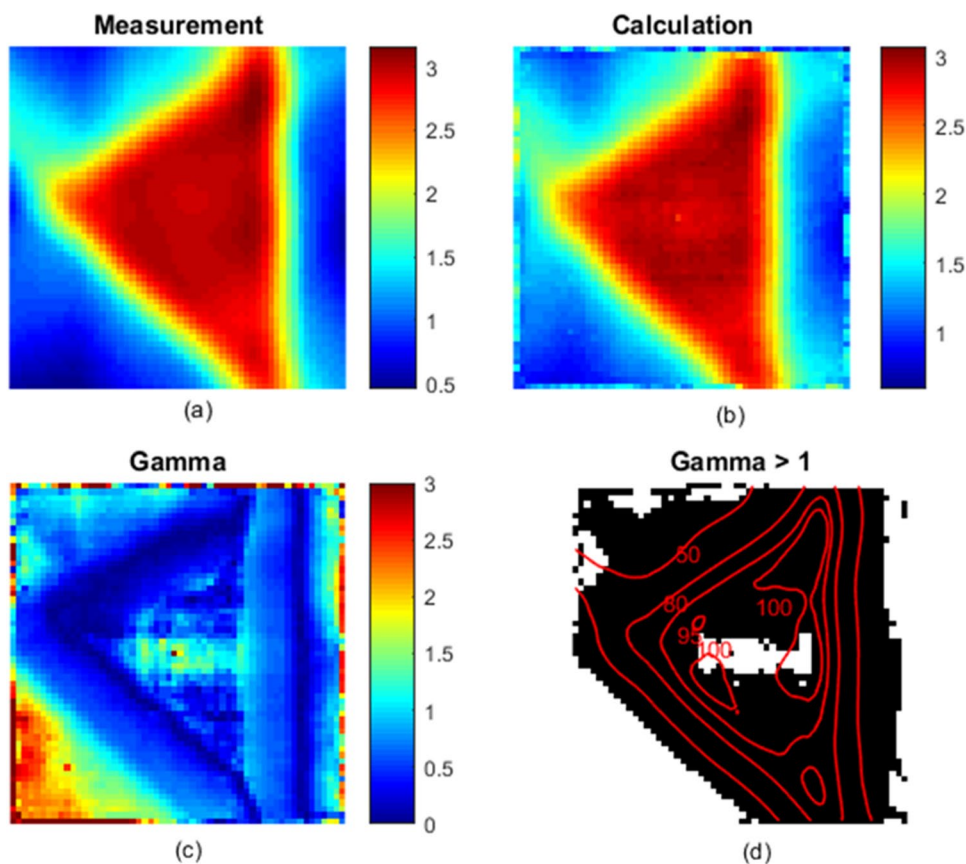
The mean pass rate for the six film pieces is 95% which is acceptable in IMRT verifications [32]. It is in accordance with the pass rate criteria presented by the developers of Marvin phantom [8]. Figure 7 shows the measured and calculated dose distributions as well as the obtained gamma indices and binary illustration of the failed pixels for film number 4 with the worst performance. Because the significant failed pixels were within the high dose, high dose gradient region, the confidence limit of 10% / 2 mm DTA, in accordance with Palta et al. [33], was tested. Exclusion of 1-mm film border resulted in a 96% pass rate that can be interpreted as another confirmation for suitability of the phantom design and material selection.

Some of the limitations of the study can be summarized as follows. Competency of the phantom in nuclear medicine applications was not investigated. However, trend of the attenuation coefficient curve versus energy for the most prominent diagnostic and therapeutic radiopharmaceuticals was not changed for <sup>99m</sup>Tc (140 keV) and <sup>131</sup>I (373 keV) energies. It is expected that the phantom can be used for nuclear medicine evaluations, as it was done in [17], but further investigation is required. Phantom dimensions were calculated based on the healthy Iranian people, and it may differ from other populations; this may affect phantom usage for others. Unfortunately, presented printed phantom has no

**Table 6** Gamma index pass rates measured by six film pieces using 3% / 3 mm acceptance criteria within their 50% isodose curve constraint. SD standard deviation

Film number	1	2	3	4	5	6	Mean	SD
Pass rate (%)	94	95	96	93	96	98	95	2

**Fig. 7** **a** The dose measured by the film number 4 (Gy), **b** the corresponding TPS calculated dose distribution (Gy), **c** calculated Gamma index, **d** the whitened regions with gamma indices more than unity. In addition, the calculated isodose lines of 100%, 95%, 80%, and 50% are superimposed on the figure



insertion for ion chambers, but the flexibility of the phantom geometry can make it possible in the future.

## 4 Conclusion

An anthropomorphic H&N phantom was designed and manufactured using a 3D printer. The phantom was designed as a hollow shell to be filled with different 3D-printed organs and detectors to make it suitable for radiation dosimetry in radiotherapy and nuclear medicine applications. This design has the required flexibility based on usage, detector variety, and resolution selection, but other phantoms like Alderson Radiation Therapy phantom with solid structure does not provide it. It incorporates TLD and film holders for the dosimetry of several organs of interest. To the best of the author's knowledge, this was the first study that used PLA as a substitute for the spongy bone tissue and showed its applicability. Attenuation properties of the selected materials were checked through MC calculations. Good agreement between the CT number values of the manufactured phantom and a real patient confirmed the phantom material selection. Gamma analysis of the calculated and measured radiation dose distributions in an IMRT plan using Gafchromic EBT2 films proved the feasibility of using MIHAN in radiotherapy

plan verification workflow. Future studies can evaluate the suitability of the MIHAN phantom for stereotactic radiosurgery (SRS) or proton therapy purposes using gel dosimeters. Investigations are necessary in future works to check if this phantom is also suitable for audit purposes in radiotherapy departments or not.

**Acknowledgements** We would like to thank Ms. Farahnaz Rahimi for providing suitable CT images.

## Declarations

**Conflict of interest** The authors declare no competing interests.

## References

- White DR, Booz J, Griffith RV, Spokas JJ, Wilson IJ (1989) Tissue substitutes in radiation dosimetry and measurement. *J Int Comm Radiat Units Meas (ICRU) Rep 44 os23*. <https://doi.org/10.1093/jicru/os23.1.Report44>
- Hermosilla A, Diaz Londono G, García M, Ruíz F, Andrade P, Pérez A (2014) Design and manufacturing of anthropomorphic thyroid-neck phantom for use in nuclear medicine centres in Chile. *Radiat Prot Dosim* 162:508–514. <https://doi.org/10.1093/rpd/ncu022>



3. Alqahtani MS, Lees JE, Bugby SL, Samara-Ratna P, Ng AH, Perkins AC (2017) Design and implementation of a prototype head and neck phantom for the performance evaluation of gamma imaging systems. *EJNMMI Phys* 4:19. <https://doi.org/10.1186/s40658-017-0186-3>
4. Mehdizadeh Naderi S, Sina S, Karimipoorfarid M, Lotfalizadeh F, Entezarmahdi M, Moradi H, Faghihi R (2015) Design and fabrication of a multipurpose thyroid phantom for medical dosimetry and calibration. *Radiat Prot Dosim* 168:503–508. <https://doi.org/10.1093/rpd/ncv359>
5. Radaideh KM, Matalqah LM, Tajuddin A, Lee WF, Bauk S, Munem EEA (2013) Development and evaluation of a Perspex anthropomorphic head and neck phantom for three dimensional conformal radiation therapy (3D-CRT). *J Radiother Pract* 12:272–280. <https://doi.org/10.1017/S1460396912000453>
6. Gopishankar N, Vivekanandhan S, Rath G, Laviraj M, Senthilkumaran S, Kale S, Thulkar S, Bisht R, Subramani V (2013) Indigenously developed multipurpose acrylic head phantom for verification of IMRT using film and gel dosimetry. *J Appl Clin Med Phys* 14:62–76. <https://doi.org/10.1120/jacmp.v14i2.4041>
7. Molineu A, Followill DS, Balter PA, Hanson WF, Gillin MT, Huq MS, Eisbruch A, Ibbott GS (2005) Design and implementation of an anthropomorphic quality assurance phantom for intensity-modulated radiation therapy for the Radiation Therapy Oncology Group. *Int J Radiat Oncol Biol Phys* 63:577–583. <https://doi.org/10.1016/j.ijrobp.2005.05.021>
8. Aitkenhead AH, Rowbottom CG, Mackay RI (2013) Marvin: an anatomical phantom for dosimetric evaluation of complex radiotherapy of the head and neck. *Phys Med Biol* 58:6915. <https://doi.org/10.1088/0031-9155/58/19/6915>
9. Webster GJ, Hardy MJ, Rowbottom CG, Mackay RI (2008) Design and implementation of a head-and-neck phantom for system audit and verification of intensity-modulated radiation therapy. *J Appl Clin Med Phys* 9:46–56. <https://doi.org/10.1120/jacmp.v9i2.2740>
10. Beaumont T, Ideias PC, Rimlinger M, Broggio D, Franck D (2017) Development and test of sets of 3D printed age-specific thyroid phantoms for 131I measurements. *Phys Med Biol* 62:4673. <https://doi.org/10.1088/1361-6560/aa6514>
11. Han Y, Lee SB, Shin EH, Kim JK, Ju SG, Yoon M, Ahn YC, Lim C, Jeong HK, Oh HJ Development of a head and neck phantom for remote-audit program of IMRT treatment. In: *World Congress on Medical Physics and Biomedical Engineering 2006, IFMBE Proceedings, 2007*. Springer, Berlin, Heidelberg, pp 2020–2023. [https://doi.org/10.1007/978-3-540-36841-0\\_507](https://doi.org/10.1007/978-3-540-36841-0_507)
12. Ibbott G, Beach M, Maryanski M (2002) An anthropomorphic head phantom with a BANG polymer gel insert for dosimetric evaluation of IMRT treatment delivery. *International Atomic Energy Agency (IAEA)*
13. Atom Max dental & diagnostic head phantom. <http://www.cirsinc.com/products/all/35/atom-max-dental-and-diagnostic-head-phantom/>. 2018
14. IMRT head and neck phantom. <http://www.cirsinc.com/products/all/11/imrt-head-and-neck-phantom/>. 2018
15. Alssabbagh M, Tajuddin AA, Abdulmanap M, Zainon R (2017) Evaluation of 3D printing materials for fabrication of a novel multi-functional 3D thyroid phantom for medical dosimetry and image quality. *Rad Phys Chem* 135:106–112. <https://doi.org/10.1016/j.radphyschem.2017.02.009>
16. Mayer R, Liacouras P, Thomas A, Kang M, Lin L, Simone CB (2015) 3D printer generated thorax phantom with mobile tumor for radiation dosimetry. *Rev Sci Instrum* 86:074301. <https://doi.org/10.1063/1.4923294>
17. Hariri Tabrizi S, Ramezani M, Feghhi SAH, Geramifar P (2020) In vitro evaluation of an iodine radionuclide dosimeter (IRD) for continuous patient monitoring. *Med Biol Eng Compu* 58:763–769. <https://doi.org/10.1007/s11517-020-02129-5>
18. Lee C, Lee C, Park SH, Lee JK (2006) Development of the two Korean adult tomographic computational phantoms for organ dosimetry. *Med phys* 33:380–390. <https://doi.org/10.1118/1.2161405>
19. Nguyen TT, Yeom YS, Kim HS, Wang ZJ, Han MC, Kim CH, Lee JK, Zankl M, Petoussi-Hens N, Bolch WE (2015) Incorporation of detailed eye model into polygon-mesh versions of ICRP-110 reference phantoms. *Phys Med Biol* 60:8695
20. Wagner H (2002) Reinforcement. *Encyclopedia of Polymer Science and Technology*
21. Khan FM, Gibbons JP (2014) *Khan's the physics of radiation therapy*. Lippincott Williams & Wilkins
22. Kumar R, Sharma S, Deshpande S, Ghadi Y, Shaiju V, Amols H, Mayya Y (2010) Acrylonitrile butadiene styrene (ABS) plastic-based low cost tissue equivalent phantom for verification dosimetry in IMRT. *J Appl Clin Med Phys* 11:24–32. <https://doi.org/10.1120/jacmp.v11i1.3030>
23. Negus IS, Holmes RB, Jordan KC, Nash DA, Thorne GC, Saunders M (2016) Development of a 3D printed subresolution sandwich phantom for validation of brain SPECT analysis. *Med phys* 43:5020–5027. <https://doi.org/10.1118/1.4960003>
24. Cember H (1969) *Introduction to health physics*. Introduction to health physics
25. Sheikh-Bagheri D, Rogers D (2002) Monte Carlo calculation of nine megavoltage photon beam spectra using the BEAM code. *Med phys* 29:391–402. <https://doi.org/10.1118/1.1445413>
26. Hsieh J Computed tomography: principles, design, artifacts, and recent advances. In: 2009. SPIE Bellingham, WA,
27. Aluminum attenuation coefficients. <https://physics.nist.gov/PhysRefData/XrayMassCoef/ElemTab/z13.html>. 2018
28. Water Attenuation coefficients. <https://physics.nist.gov/PhysRefData/XrayMassCoef/ComTab/water.html>. 2018
29. Devic S, Seuntjens J, Sham E, Podgorsak EB, Schmidtlein CR, Kirov AS, Soares CG (2005) Precise radiochromic film dosimetry using a flat-bed document scanner. *Med phys* 32:2245–2253. <https://doi.org/10.1118/1.1929253>
30. Hong TS, Tomé WA, Harari PM (2012) Heterogeneity in head and neck IMRT target design and clinical practice. *Radiother Oncol* 103:92–98
31. Low DA, Dempsey JF (2003) Evaluation of the gamma dose distribution comparison method. *Med phys* 30:2455–2464. <https://doi.org/10.1118/1.1598711>
32. Alber M, Broggi S, De Wagter C, Eichwurz I, Engström P, Fiorino C, Georg D, Hartmann G, Knöös T, Leal A (2008) Guidelines for the verification of IMRT. *ESTRO booklet 7*
33. Palta J, Kim S, Li JG, Liu C (2003) Tolerance limits and action levels for planning and delivery of IMRT. In: *Intensity-modulated radiation therapy: the state of the art*. Medical Physics, Madison, Wisconsin,

**Publisher's note** Springer Nature remains neutral with regard to jurisdictional claims in published maps and institutional affiliations.



**Mohammad Ahmadi** He received his BS degree in biomedical engineering. This study was for fulfillment of his MS thesis in medical radiation engineering at Shahid Beheshti University of Tehran. He is now working on development of the current system.



**Sanaz Hariri Tabrizi** She received the BS degree in biomedical engineering in 2005 and the MS and PhD degrees in medical radiation engineering in 2008 and 2013, respectively. She is now an assistant professor at Shahid Beheshti University.



**Meysam Ramezani Anarestani** He received his BS degree in biomedical engineering. This study was for fulfillment of his MS thesis in radiation applications at Shahid Beheshti University of Tehran. He is now working on the design and construction of the dosimeters.



**Zohreh Azma** She received the BS degree in applied physics in 2005 and her MS degree in medical radiation engineering in 2008. Her main research fields are medical physics, radiation dosimetry in the clinical practice, quantitative imaging, molecular imaging, and Monte Carlo simulations. Mohammad Ahmadi He received his BS degree in biomedical engineering. This study was for fulfillment of his MS thesis in medical radiation engineering at Shahid Beheshti University of Tehran. He is now working on development of the current system.